Nanowire-Directed Templating Synthesis of Metal−Organic Framework Nanofibers and Their Derived Porous Doped Carbon Nanofibers for Enhanced Electrocatalysis

Wang Zhang, Zhen-Yu Wu, Hai-Long Jiang, and Shu-Hong Yu*

Division of Nanomaterials and Chemistry, Hefei National Laboratory for Physical Sciences at Microscale, Collaborative Innovation Center of Suzhou Nano Science and Technology, Department of Chemistry, University of Science and Technology of China, Hefei, Anhui 230026, P. R. China

S *Supporting Information*

ABSTRACT: A nanowire-directed templating synthesis of metal−organic framework (MOF) nanofibers has been demonstrated, where ultrathin tellurium nanowires (TeNWs) with excellent dispersivity can act as templates for directed growth and assembly of ZIF-8 nanocrystals (one typical MOF), resulting in the formation of uniform ZIF-8 nanofibers. The as-obtained ZIF-8 nanofibers can be conveniently converted into highly porous doped carbon nanofibers by calcination. Compared with bulk porous carbon by direct carbonization of MOF crystals, these doped carbon nanofibers exhibit complex network structure, hierarchical pores, and high surface area. Further doped by phosphorus species, the co-doped carbon nanofibers exhibit excellent electrocatalytic performance for oxygen reduction reaction, even better than the benchmark Pt/C catalyst.

Metal−organic frameworks (MOFs) are a family of crystalline porous solids with supramolecular structure consisting of metal ions and organic ligands linked together by coordination bonds.[1] Very recently, MOF-derived carbon materials have attracted great interest for energy conversion and storage applications due to their exceptionally high specific surface area and controllable pore textures.[2] To date, many studies have reported that multiple types of MOFs with other carbon sources could be transformed into amorphous micro-porous carbons by direct pyrolysis under an inert atmosphere without any activation.[3] Unfortunately, the main effort in this research field is mainly devoted to MOF microcrystals or nanocrystals, and it lacks rational design for control of the shape and size of the resultant materials. In the carbonization process, the MOF crystals are converted into bulk carbon powder due to high temperature, which would result in reduced effective special surface area. For this reason, although a few bulk MOF-derived microporous carbons as electrocatalysts have been introduced in fuel cell fields,[4] most of them exhibit worse electrochemical activity than commercial Pt/C catalyst for cathode oxygen reduction reaction (ORR).

Based on the inherent driving force for crystallization, MOF crystals tend to present a unique morphology and hard to change. Therefore, searching for new strategies for controlling the dimensions of the MOF crystals has attracted a lot of concerns.[5] During the past few years, a variety of strategies toward higher-order MOF superstructures have been successfully developed.[6] For instance, Furukawa et al. reported a rapid method to spatially control the nucleation site to form mesoscopic architecture MOFs in both two and three dimensions.[6d] Maspoch et al. demonstrated a spray-drying strategy to construct hollow multicomponent MOF superstructures.[6e] However, the MOF assemblies composed of nanocrystals as building blocks in one dimension remain largely unexplored.

With our continued efforts, ultrathin tellurium nanowires (TeNWs) have been proven to be excellent templates for the formation of one-dimensional (1D) architectures such as carbonaceous nanofibers, noble metal nanowires and nano-tubes.[7] Therefore, TeNWs are chosen as hard templates to induce the nucleation and growth of a prototypical zeolite-type MOF, $Zn(MeIM)_2$ (ZIF-8; MeIM = 2-methylimidazole)[8] in this work. By simply introducing the TeNWs template into the precursor solutions, the uniform ZIF-8 nanofibers with high aspect ratio and controllable diameters can be achieved, due to the attachment of ZIF-8 nuclei and nanocrystals onto the active surface of the TeNWs. Furthermore, we elaborately choose such 1D ZIF-8 nanocrystal assembly as precursor, which not only can be used to achieve high specific surface area and have rich nitrogen content but also can generate nanofibrous morphology for improving electron conduction and mass transport, and we successfully obtain highly porous doped carbon nanofibers with subsequent thermal treatment process. Such doped carbon nanofibers as ORR catalyst in fuel cell field have been carefully investigated. Upon doping with a little bit of phosphorus (P) species, the resultant catalyst shows excellent electrocatalytic performance, even better activity and durability as well as methanol tolerance than those of the benchmark Pt/C catalyst under the same experimental conditions.

The formation process from TeNWs to ZIF-8 nanofibers and final porous doped carbon nanofibers is illustrated in Scheme 1 (see Supporting Information for details). In the first step, ultrathin TeNWs were obtained under hydrothermal conditions, and well-defined Te@ZIF-8 was subsequently prepared by mixing zinc nitrate and MeIM in methanol solution of TeNWs at room temperature. To avoid the as-obtained nanofibers collapse when evaporating off the solvent, the freeze-drying technique was employed to maintain the 3D scaffold structure of ZIF-8

Scheme 1. Illustration of the Nanowire-Directed Templating Synthesis of ZIF-8 Nanofibers and Derived Porous Doped Carbon Nanofibers
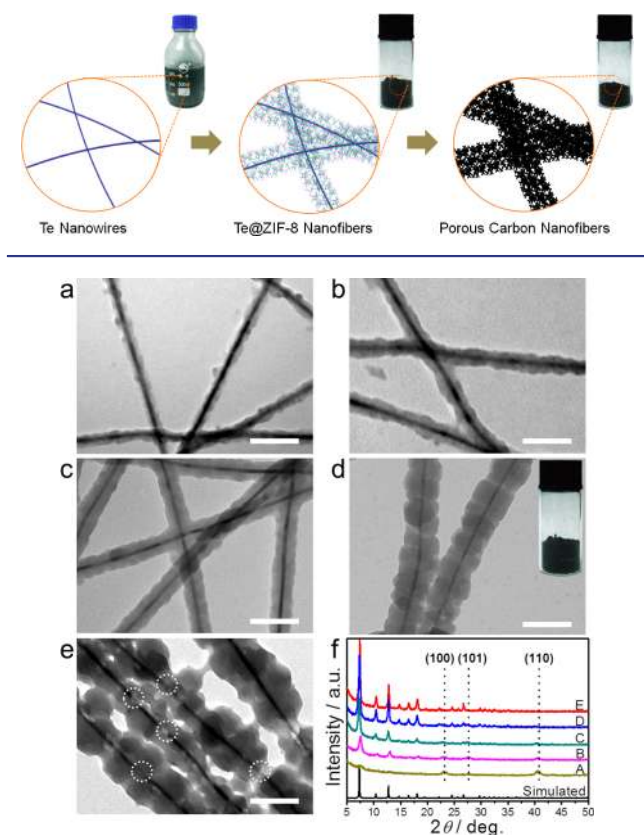

Figure 1. (a−e) TEM images of as-prepared Te@ZIF-8 by regulating the amounts of precursors. (a−e) corresponding to samples A−E; the average diameter of A− E corresponds to 27, 36, 45, 73, and 95 nm, respectively; scale bar: 100 nm. Inset in (d) shows the photo of the sample D. (f) PXRD patterns of as-prepared samples A−E.

Figure 2. (a) TEM image of Z8-Te-1000. Inset in right shows the photo of the sample. (b) Magnified TEM image of Z8-Te-1000. (c) HRTEM image of Z8-Te-1000. (d) N_2 sorption isotherms of Z8-Te-1000 and Z8-1000. Inset shows the pore size distribution of Z8-Te-1000 by BJH.

nanofibers at microscale. Finally, the dried ZIF-8 nanofibers powder was transferred to a temperature-programmed furnace under nitrogen gas flow, heat treated at 200 °C for 6 h, and then pyrolyzed at 1000 °C for 8 h, resulting in the formation of highly porous doped carbon nanofibers.

As shown in Figures 1a−e and S1a−e, which were labeled corresponding by samples A−E, crystalline ZIF-8 nanocrystals can be induced and attached onto the outer surface of TeNWs under optimum synthetic conditions, resulting in the formation of 1D nanofibrous structure. The powder X-ray diffraction (PXRD) patterns confirm that all samples are the composites of Te and ZIF-8 (Figure 1f). The main peaks and relative intensity are in agreement with those of simulated results, confirming the formation of pure crystalline ZIF-8 phase. Meanwhile, it can be seen that the peaks at two theta values of 23.1, 27.8, and 40.5 can be indexed to (100), (101), and (110) crystal planes of the Te phase (JCPDF card number: 36-1452) respectively, revealing that TeNWs are remained. With changing the concentrations of precursor, the diameter of ZIF-8 nanofibers can be well-tuned from 27 to 73 nm corresponding with samples A−D, respectively. Further increasing the concentration, the TEM image of sample E shows that TeNWs has been partly broken, and the ZIF-8 nanofibers completely disconnect finally (Figure S1f), which is attributed to too large sizes of ZIF-8 nanocrystals. Furthermore, it is obvious that the peak intensity of PXRD
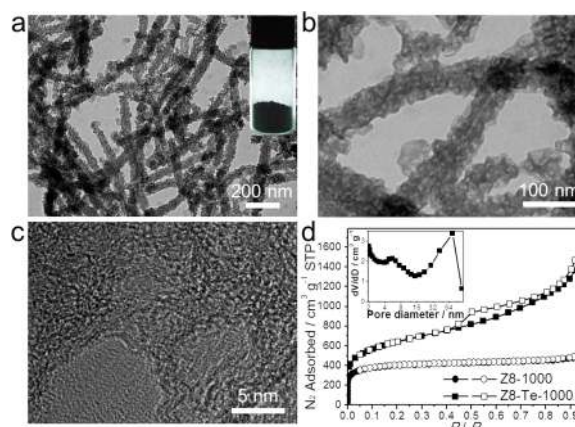
patterns from samples A−E increase gradually accompanying by the raise in diameter of ZIF-8 nanofibers, revealing that the concentration of precursor is a key parameter that significantly affects the crystallinity as well as the diameter of ZIF-8 nanofibers. On the other hand, the content of TeNWs in the solution also plays another important role in preparing uniform ZIF-8 nanofibers. When one-half concentrations (see Figure S2 for details) of Te templates are used and the concentration of precursor is remained, a significant amount of ZIF-8 nanocrystals will independently nucleate and grow in the solution. On the contrary, the outer surface of each Te nanowire is incompletely coated by ZIF-8 nanocrystals (see Figure S2). TEM images confirm that ZIF-8 nanocrystals preferentially coated on the surface of TeNWs and formed in solution until completely covered, implying the effective template role of TeNWs.

In the next step, we chose the sample D for the heat treatment process because of its undamaged nanofibrous morphology and better crystallinity. The TEM image in Figure 2a shows the shape of the initial ZIF-8 nanofibers as self-sacrificial templates can be maintained well in the final hollow carbon product after carbonization. The resultant product (referred to as Z8-Te-1000 hereafter, Z8 is ZIF-8 abbreviation and 1000 shows treatment temperature) derived from the sample D shows clearly nanosized hollow fibrous morphology with uniform diameter of ∼50 nm (Figure 2b). For comparison, the ZIF-8 nanocrystals were directly pyrolyzed under the same conditions. As shown in Figure S3a,d, the resultant carbon (referred to as Z8-1000 hereafter) retains initial ZIF-8 template morphology. However, these nanoparticles aggregated in large amounts to form the microsized particles with irregular shape after heat treatment. The significant difference in volume can be clearly observed between Z8-Te-1000 and Z8-1000 under the same weight (Figure S4), which further confirmed the viewpoints of the aggregation of unassembled ZIF-8 nanocrystals derived carbon nanoparticles at high temperature. The abundant disordered graphene layer can be observed in the high-resolution TEM (HRTEM) image of Z8-Te-1000 (Figure 2c), which agrees with the results of carbonization of ZIF-8 directly reported previously.[3c,e,h] The PXRD patterns and Raman spectra also confirm that the local carbon structures of all synthesized samples contain both graphitic and disordered carbon atoms (Figures S5 and S6).[3c,e] No obvious diffraction peaks of impurities could be observed, suggesting that TeNWs, similar

to metal Zn, can be vaporized completely under the high-temperature conditions corresponding with the observation of the TEM images. The contents of residual Te (0.54 wt %) and Zn (0.69 wt %) in Z8-Te-1000 were measured by inductively coupled plasma mass spectrometry.

N_2 sorption isotherms of nanofibrous doped carbon and bulk doped carbon are shown in Figure 2d. The curve of Z8-1000 shows a type-I isotherm,[3c,e] revealing a typical micropore characteristic. Dramatically, Z8-Te-1000 derived from ZIF-8 nanocrystals assembled nanofibers exhibits a type-IV curve with a pronounced hysteresis loop, suggesting the formation of mesoporous structure due to residual channel after vaporized TeNWs and the porous network structure consisting of disordered nanofibers with uniform diameter. According to the Barrett–Joyer–Halenda (BJH) model, the inset in Figure 2d shows that Z8-Te-1000 has a relatively broad meso- to macropore diameters with a maximum frequency near 5.5 and 75 nm corresponding with the result of TEM measurement. The specific surface areas estimated by the Brunauer–Emmett–Teller (BET) method and total pore volume of Z8-Te-1000 and Z8-1000 are 2270 m^2 g^{-1} (2.93 cm^3 g^{-1}) and 1481 m^2 g^{-1} (0.76 cm^3 g^{-1}), respectively.

Such porous doped carbon nanofibers can be utilized in fuel cell as electrocatalyst for ORR. In order to further improve the electrochemical activity, P element was introduced into this system by reannealing with triphenylphosphine in nitrogen atmosphere, because the process of P atoms doped into carbon matrix is one of the most effective ways to create competent ORR catalytic active sites.[9] The porous carbon nanofiber with P-doping was labeled by P-Z8-Te-1000, and bulk carbon with P-doping was labeled by P-Z8-1000 for comparison. The morphology of these two samples both retained after the reannealing process (Figure S3b,c,e,f). The S_{BET} and total pore volume of these catalysts after P-doping are 1417 m^2 g^{-1} and 1.21 cm^3 g^{-1} (P-Z8-Te-1000) and 897 m^2 g^{-1} and 0.40 cm^3 g^{-1} (P-Z8-1000), respectively (Figure S7 and Table S1). Pore features of the catalysts with P-doping exhibit similar structures to those of catalysts without P-doping. However, compared with the samples before involving P, the both samples of P-Z8-1000 and P-Z8-Te-1000 show a relative low BET surface that attributes to partly collapsing and blocking the pore in the matrix carbon.

The X-ray photoelectron spectroscopy (XPS) confirmed that all four samples reveal a predominant peak at 284.7 eV corresponding to C 1s, at 531.4 eV to O 1s, and at 399.5 eV to N 1s, indicating the presence of C, O, and N elements (Figure S8). Meanwhile, a weak peak at 133.1 eV attributes to P 2p in the spectra of P-Z8-1000 and P-Z8-Te-1000, revealing that P atoms are successfully incorporated in the carbon matrix. The presence of oxygen can be attributed to residual polyvinylpyrrolidone in the synthesis step of TeNWs and oxygen-containing small molecules (e.g., water and dioxide carbon) adsorbed on such porous carbon.[10] The high-resolution N 1s XPS spectra reveal the presence of three types bonding state of the N atom in these catalysts (Figure S9), suggesting that the resultant products are N-doped carbon. The results exhibit a similar ratio of the content of these three types of N in all samples, which is attributed to the same derivation of MeIM in ZIF-8 framework after the same high-temperature treatment process. In the high-resolution P 2p spectra, the peak at 132.7 and 133.8 eV can be assigned to P–C and P–O bonding, respectively (Figure S10). Interestingly, the P-doping level of P-Z8-Te-1000 (0.51 at %) is very close to that of P-Z8-1000 (0.48 at %). However, the content of P–C bond of
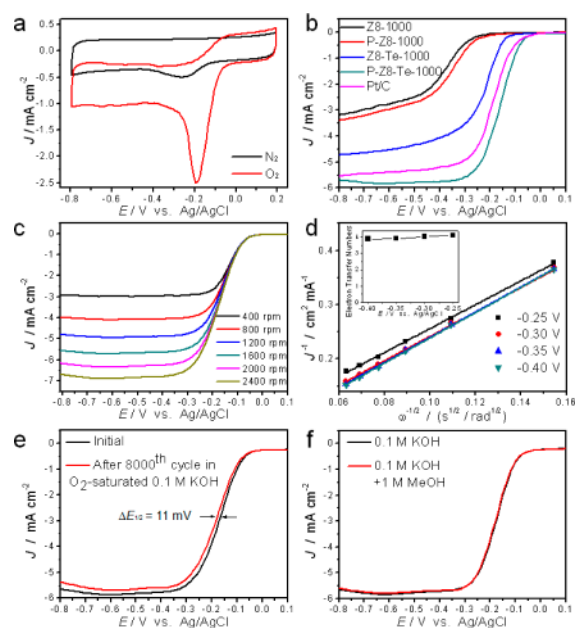

Figure 3. (a) CV curves of P-Z8-Te-1000. (b) Linear sweep voltammetry (LSV) curves of all catalysts in O_2-saturated 0.1 M KOH with a sweep rate of 10 mV s^{-1} and electrode rotation speed of 1600 rpm. (c) LSV curves for P-Z8-Te-1000 at the different rotation rate. (d) Kouteck–Levich plots of P-Z8-Te-1000 derived from RDE data. (e) LSV curves of P-Z8-Te-1000 after 8000 potential cycles in O_2-saturated solution. (f) LSV curves of P-Z8-Te-1000 in 0.1 M KOH without (black curve) and with (red curve) 1 M MeOH (catalyst loading ~0.1 mg cm^{-2}).

P-Z8-Te-1000 (70 at %) is much higher than that of P-Z8-1000 (36.9 at %), while the content of P–O bond of P-Z8-Te-1000 (30 at %) is much lower than that of P-Z8-1000 (63.1 at %). The presence of the P–C covalent bond with high content confirms more effective P atoms doping into the carbon lattice owing to nanofibrous morphology, highly effective S_{BET} as well as hierarchical pore structure of the doped carbon nanofibers.

A commercial Pt/C (20 wt % Pt on Vulcan carbon black, Johnson Matthey) catalyst was tested under the same conditions for comparison. We performed cyclic voltammetry (CV) and rotating disk electrode (RDE) measurements to assess the ORR performances of the catalysts. The CV curves for all samples exhibit a pronounced peak in O_2-saturated solution, implying that these catalysts possess ORR activity (Figures 3a and S11a–c). The ORR performances of these five samples were then further investigated (Figure 3b). Z8-1000 exhibits very poor ORR activity (onset potential of ~ −0.25 V and half-wave potential of ~ −0.391 V), and the performance of P-Z8-1000 has little improvement (onset potential of ~ −0.22 V and half-wave potential of ~ −0.367 V). Although these two catalysts possess highly microporous structure, the effective BET surface of the micrometer-sized (even dozens of micrometers) bulk carbon is very low, and it is even lower after doping with P. On the contrary, the nanofibrous carbon (Z8-Te-1000) with abundant effective BET surface dramatically promotes the catalytic activity. The ORR performance of Z8-Te-1000 (onset potential of ~ −0.14 V and half-wave potential of ~ −0.226 V) exhibits much better activity than those of Z8-1000 and P-Z8-1000 and is close to the commercial Pt/C catalyst. Remarkably, LSV curve reveals the high ORR activity of P-Z8-Te-1000 with an onset potential of ~ −0.07 V and half-wave potential of ~ −0.161 V, which is even better active than the commercial Pt/C catalyst (onset potential

of ~ −0.08 V and half-wave potential of ~ −0.192 V) with the exactly consistent loading (~0.1 mg cm^{-2}) in the completely same test conditions, suggesting that more active sites were created by doping P element. We also explored the ORR activity of the samples prepared at different temperatures (Figure S12). Clearly, the increase of carbonization temperature leads the great improvement of the ORR performance. The results confirm that P-Z8-Te-1000 exhibits the best catalytic activity. Significantly, compared to other top electrocatalysts (including doped carbon-based metal-free catalysts and MOF-derived catalysts), P-Z8-Te-1000 is also one of the best highly active ORR catalysts in an alkaline medium (Table S1).

For further assessment of the pathway of ORR for all samples, the RDE measurements were performed at various rotating speeds at a scan rate of 10 mV s^{-1} under O$_2$-saturated system. The results reveal an electron transfer number of ~4.0 at −0.25 to −0.4 V for P-Z8-Te-1000 catalyst (Figure 3d and Table S1), similar to that of Pt/C catalyst and much higher than those of other reference catalysts. Except for excellent ORR activity of the P-Z8-Te-1000, it also exhibits good stability as well as superior methanol tolerance. For comparison, P-Z8-Te-1000 and Pt/C were cycled from −0.4 to 0 V at 100 mV s^{-1} in O$_2$-saturated 0.1 M KOH solutions (Figures 3e and S13a). After continuous potential cycles for 8000 times, the half-wave potential $E_{1/2}$ of P-Z8-Te-1000 exhibited a bit of a negative shift of ~11 mV, which is much lower than that of Pt/C catalyst with ~49 mV negative shift, indicating the P-Z8-Te-1000 has much better stability than the commercial Pt/C catalyst. On the other hand, it is well-known that noble metal Pt can be poisoned by methanol (Figure S13b). Here, no obvious variation with the LSV curve of P-Z8-Te-1000 was observed after addition of methanol, totally different from Pt/C catalyst (Figure 3f), suggesting that it is a promising candidate as cathode catalyst employed in direct methanol alkaline fuel cell.

In summary, we report a new strategy for controllable synthesis of 1D ZIF-8 nanofibers by using TeNWs as a template, which can be subsequently transformed into doped carbon nanofibers by calcination. Such doped carbon materials with hierarchical pore structure and nanofibrous morphology can be used as efficient electrocatalyst for ORR in alkaline media, exhibiting excellent electrocatalytic activity and long-term durability as well as good resistance to methanol crossover effects. The present work suggests that such rational design and synthesis of co-doped carbon nanofibers possess highly effective S_{BET} and hierarchical porous feature, which obviously improve the accessibility of the molecules and ions to the catalytic active sites and shorter diffusion path lengths facilitating the ORR process. It is expected that this nanowire-directed templating method will provide new opportunities for rational design and synthesis of MOF nanocrystal assemblies and their derived porous carbon or metal oxide materials by using other functional MOFs.

ASSOCIATED CONTENT

ⓈSupporting Information

Experimental details and characterization data. This material is available free of charge via the Internet at http://pubs.acs.org.

AUTHOR INFORMATION

Corresponding Author

shyu@ustc.edu.cn

Notes

The authors declare no competing financial interest.

REFERENCES

(1) (a) Yaghi, O. M.; O'Keeffe, M.; Ockwig, N. W.; Chae, H. K.; Eddaoudi, M.; Kim, J. *Nature* **2003**, *423*, 705. (b) Kitagawa, S.; Kitaura, R.; Noro, S.-i. *Angew. Chem., Int. Ed.* **2004**, *43*, 2334. (c) Furukawa, H.; Cordova, K. E.; O'Keeffe, M.; Yaghi, O. M. *Science* **2013**, *341*, 974.

(2) Sun, J.-K.; Xu, Q. *Energy Environ. Sci.* **2014**, *7*, 2071.

(3) (a) Liu, B.; Shioyama, H.; Akita, T.; Xu, Q. *J. Am. Chem. Soc.* **2008**, *130*, 5390. (b) Liu, B.; Shioyama, H.; Jiang, H.; Zhang, X.; Xu, Q. *Carbon* **2010**, *48*, 456. (c) Jiang, H.-L.; Liu, B.; Lan, Y.-Q.; Kuratani, K.; Akita, T.; Shioyama, H.; Zong, F.; Xu, Q. *J. Am. Chem. Soc.* **2011**, *133*, 11854. (d) Radhakrishnan, L.; Reboul, J.; Furukawa, S.; Srinivasu, P.; Kitagawa, S.; Yamauchi, Y. *Chem. Mater.* **2011**, *23*, 1225. (e) Chaikittisilp, W.; Hu, M.; Wang, H.; Huang, H.-S.; Fujita, T.; Wu, K. C. W.; Chen, L.-C.; Yamauchi, Y.; Ariga, K. *Chem. Commun.* **2012**, *48*, 7259. (f) Hu, M.; Reboul, J.; Furukawa, S.; Torad, N. L.; Ji, Q.; Srinivasu, P.; Ariga, K.; Kitagawa, S.; Yamauchi, Y. *J. Am. Chem. Soc.* **2012**, *134*, 2864. (g) Yang, S. J.; Kim, T.; Im, J. H.; Kim, Y. S.; Lee, K.; Jung, H.; Park, C. R. *Chem. Mater.* **2012**, *24*, 464. (h) Torad, N. L.; Hu, M.; Kamachi, Y.; Takai, K.; Imura, M.; Naito, M.; Yamauchi, Y. *Chem. Commun.* **2013**, *49*, 2521.

(4) (a) Proietti, E.; Jaouen, F.; Lefèvre, M.; Larouche, N.; Tian, J.; Herranz, J.; Dodelet, J.-P. *Nat. Commun.* **2011**, *2*, 416. (b) Palaniselvam, T.; Biswal, B. P.; Banerjee, R.; Kurungot, S. *Chem.—Eur. J.* **2013**, *19*, 9335. (c) Zhang, P.; Sun, F.; Xiang, Z.; Shen, Z.; Yun, J.; Cao, D. *Energy Environ. Sci.* **2014**, *7*, 442. (d) Aijaz, A.; Fujiwara, N.; Xu, Q. *J. Am. Chem. Soc.* **2014**, *136*, 6790.

(5) (a) Carné-Sánchez, A.; Imaz, I.; Stylianou, K. C.; Maspoch, D. *Chem.—Eur. J.* **2014**, *20*, 5192. (b) Furukawa, S.; Reboul, J.; Diring, S.; Sumida, K.; Kitagawa, S. *Chem. Soc. Rev.* **2014**, *43*, 5700.

(6) (a) Ameloot, R.; Vermoortele, F.; Vanhove, W.; Roeffaers, M. B. J.; Sels, B. F.; De Vos, D. E. *Nat. Chem.* **2011**, *3*, 382. (b) Ostermann, R.; Cravillon, J.; Weidmann, C.; Wiebcke, M.; Smarsly, B. M. *Chem. Commun.* **2011**, *47*, 442. (c) Kuo, C.-H.; Tang, Y.; Chou, L.-Y.; Sneed, B. T.; Brodsky, C. N.; Zhao, Z.; Tsung, C.-K. *J. Am. Chem. Soc.* **2012**, *134*, 14345. (d) Reboul, J.; Furukawa, S.; Horike, N.; Tsotsalas, M.; Hirai, K.; Uehara, H.; Kondo, M.; Louvain, N.; Sakata, O.; Kitagawa, S. *Nat. Mater.* **2012**, *11*, 717. (e) Carné-Sánchez, A.; Imaz, I.; Cano-Sarabia, M.; Maspoch, D. *Nat. Chem.* **2013**, *5*, 203. (f) Yanai, N.; Sindoro, M.; Yan, J.; Granick, S. *J. Am. Chem. Soc.* **2013**, *135*, 34.

(7) (a) Qian, H.-S.; Yu, S.-H.; Luo, L.-B.; Gong, J.-Y.; Fei, L.-F.; Liu, X.-M. *Chem. Mater.* **2006**, *18*, 2102. (b) Liang, H.-W.; Liu, S.; Gong, J.-Y.; Wang, S.-B.; Wang, L.; Yu, S.-H. *Adv. Mater.* **2009**, *21*, 1850. (c) Liang, H.-W.; Wang, L.; Chen, P.-Y.; Lin, H.-T.; Chen, L.-F.; He, D.; Yu, S.-H. *Adv. Mater.* **2010**, *22*, 4691. (d) Liang, H.-W.; Guan, Q.-F.; Chen, L.-F.; Zhu, Z.; Zhang, W.-J.; Yu, S.-H. *Angew. Chem., Int. Ed.* **2012**, *51*, 5101. (e) Li, H.-H.; Zhao, S.; Gong, M.; Cui, C.-H.; He, D.; Liang, H.-W.; Wu, L.; Yu, S.-H. *Angew. Chem., Int. Ed.* **2013**, *52*, 7472. (f) Liang, H.-W.; Liu, J.-W.; Qian, H.-S.; Yu, S.-H. *Acc. Chem. Res.* **2013**, *46*, 1450.

(8) (a) Huang, X.-C.; Lin, Y.-Y.; Zhang, J.-P.; Chen, X.-M. *Angew. Chem., Int. Ed.* **2006**, *45*, 1557. (b) Park, K. S.; Ni, Z.; Côté, A. P.; Choi, J. Y.; Huang, R.; Uribe-Romo, F. J.; Chae, H. K.; O'Keeffe, M.; Yaghi, O. M. *Proc. Natl. Acad. Sci. U.S.A.* **2006**, *103*, 10186.

(9) (a) Liu, Z.-W.; Peng, F.; Wang, H.-J.; Yu, H.; Zheng, W.-X.; Yang, J. *Angew. Chem., Int. Ed.* **2011**, *50*, 3257. (b) Yang, D.-S.; Bhattacharjya, D.; Inamdar, S.; Park, J.; Yu, J.-S. *J. Am. Chem. Soc.* **2012**, *134*, 16127.

(10) Wu, Z.-S.; Chen, L.; Liu, J.; Parvez, K.; Liang, H.; Shu, J.; Sachdev, H.; Graf, R.; Feng, X.; Muellen, K. *Adv. Mater.* **2014**, *26*, 1450.